Article

Not peer-reviewed version

Optical and Structural Properties of Co^{2+}-Doped $CsPbI_3$ Nanocrystals Embedded in Borosilicate Glass

Wilson A. da Silva , Éder V. Guimarães * , Klever A. S. Costa , Nataly S. Moura , Jose F. Condeles , Raquel A. Domingues , Ricardo S. Silva *

Posted Date: 15 April 2026

doi: 10.20944/preprints202604.1045.v1

Keywords: $CsPbI_3$ nanocrystals; borosilicate glass; melt-quenching; tetrahedral crystal field; excitonic emission

 doi:10.20944/preprints202604.1045.v1

Article

Optical and Structural Properties of Co^{2+}-Doped $CsPbI_3$ Nanocrystals Embedded in Borosilicate Glass

Wilson A. da Silva [1], Éder V. Guimarães [1,*], Klever A. S. Costa [1], Nataly S. Moura [1], José F. Condeles [1], Raquel A. Domingues [2] and Ricardo S. Silva [1,*]

[1] Instituto de Ciências Exatas, Naturais e Educação (ICENE), Departamento de Física, Universidade Federal do Triângulo Mineiro, 38025–180, Uberaba, MG, Brazil

[2] Instituto de Ciência e Tecnologia (ICT), Universidade Federal de São Paulo, 13083–970, São José dos Campos, SP, Brazil

* Correspondence: edervgol@gmail.com (E.V.G.); ricardo.silva@uftm.edu.br (R.S.S.)

Abstract

Co^{2+}-doped $CsPbI_3$ nanocrystals (NCs) ($CsPbI_3$:xCo, x = 0, 0.05, and 0.10 mol%) were synthesized in situ within a borosilicate glass matrix by the fusion method followed by controlled thermal treatment at 500 °C for 6–24 h. Transmission electron microscopy images showed quasi-spherical NCs formed within the glass matrix with mean diameters ranging from 6.3 to 8.4 nm, consistent with diffusion-mediated growth under glass nanoconfinement. Energy-dispersive X-ray spectroscopy confirmed the presence of Co within the NCs regions. X-ray diffraction patterns confirm the exclusive stabilization of the cubic α-phase across all compositions, with a systematic shift of the (200) reflection to greater angles with increasing Co content, evidencing B-site lattice contraction due to the substitution of Pb^{2+} by Co^{2+}. Optical absorption and photoluminescence spectra demonstrate that Co^{2+} incorporation enhances the δ-phase emission in the as-prepared condition, consistent with defect passivation, and that progressive thermal treatment stabilizes band-edge excitonic emission near ~1.74 eV without disrupting the fundamental optical response of the α-$CsPbI_3$ host. Crystal field theory and Tanabe–Sugano analysis for d^7 ions in Td symmetry yielded $\Delta = 5032$ cm^{-1} and $B = 725$ cm^{-1} in the as-prepared state, evolving to $\Delta = 4428$ cm^{-1} and $B = 805$ cm^{-1} after thermal treatment, confirming the tetrahedral coordination of Co^{2+} and significant metal–iodide covalency. These results position $CsPbI_3$:xCo NCs embedded in glass as robust platforms for glass-integrated photonic applications.

Keywords: $CsPbI_3$ nanocrystals; borosilicate glass; melt-quenching; tetrahedral crystal field; excitonic emission

1. Introduction

All-inorganic halide perovskite nanocrystals (NCs) ($CsPbX_3$, X = Cl, Br, I) have attracted considerable attention in recent decades due to their interesting optical properties and potential for technological applications in devices such as solar cells, light-emitting diodes, lasers, and photodetectors [1–6]. Among these materials, $CsPbI_3$ stands out because of its direct bandgap near 1.7 eV in the visible–near-infrared spectral region, making it a strong candidate for photovoltaic and light-emitting applications [7,8]. However, the cubic α-phase of $CsPbI_3$, which is responsible for its excellent optical properties, is metastable at room temperature and spontaneously converts into the non-perovskite orthorhombic δ-phase under ambient conditions [8,9]. This yellow δ-phase presents a wide bandgap of ~2.8 eV and poor optoelectronic performance, which severely limits the practical use of $CsPbI_3$ [9,10]. In the last decade, different stabilization strategies have been explored, including quantum confinement, compositional engineering, surface passivation, and partial ionic substitution at the B-site [11–16].

The doping of $CsPbX_3$ NCs with transition-metal (TM) ions has been explored as an approach to simultaneously modulate their structural and optical properties [17]. Among the available TM

 doi:10.20944/preprints202604.1045.v1

dopants, Co^{2+} ions ($3d^7$, high-spin) are particularly relevant due to their intense intra-3d optical transitions, whose energies and intensities are governed by crystal-field interactions and are therefore sensitive to local coordination geometry, ligand-field strength, and metal–ligand covalency [17]. This behavior has been extensively documented in chalcogenide-based NCs systems and glass–NC composites, encompassing $Bi_{2-x}Co_xS_3$, $Pb_{1-x}Co_xS$, $Zn_{1-x}Co_xO$, and $Zn_{1-x}Co_xTe$ hosts, where Co^{2+} ions serve simultaneously as functional dopants and as spectroscopic probes of local structure [18–22]. The role of Co^{2+} in halide perovskite matrices, however, remains comparatively limited, particularly within fully inorganic environments where dopant segregation and phase instability represent important constraints [23,24].

The synthesis of $CsPbX_3$ NCs within glass matrices has emerged as an effective route to circumvent the phase instability and environmental sensitivity inherent to bulk perovskite films, affording excellent control over NC size, high thermal stability, and strong resistance to moisture-induced degradation [25–29]. Near the glass transition temperature (T_g), short-range atomic mobility is sufficient to drive diffusion-limited nucleation and growth of NCs with controllable size distributions, while the rigid vitreous network suppresses bulk devitrification and macroscopic phase segregation [25–27]. Under these nanoconfinement conditions, the cubic α-$CsPbI_3$ phase can be stabilized with well-defined excitonic features and photoluminescence efficiency [26,30].

Borosilicate glasses are particularly well suited for hosting iodide perovskite NCs, owing to their low hygroscopicity, high thermal and chemical stability, and chemical compatibility with halide precursors [25,26,28]. The borosilicate network also provides a stable confinement environment in which transition-metal dopants incorporated at the B-site of the perovskite NCs can adopt tetrahedral (T_d) coordination geometries, as reported for Co^{2+} ions in chalcogenide glass–nanocrystal composites [18,20,28–32]. The crystal-field-driven optical transitions of Co^{2+} ions in T_d symmetry offer direct spectroscopic access to local coordination geometry, ligand-field strength, and metal–ligand covalency.

In this work, we report the optical and structural properties of Co^{2+}-doped $CsPbI_3$ NCs ($CsPbI_3$:xCo, x = 0, 0.05, and 0.10 mol%) synthesized in situ within a borosilicate glass matrix by the fusion method followed by controlled thermal treatment. X-ray diffraction (XRD), Transmission electron microscopy (TEM), and Energy-dispersive X-ray spectroscopy (EDX) were used to characterize the structural and morphological properties of the NCs. Optical absorption (OA) and photoluminescence (PL) spectroscopy were employed to analyze the optical behavior of the host perovskite and the Co^{2+} dopant states. Crystal field theory (CFT) and Tanabe–Sugano analysis for d^7 ions in T_d symmetry were applied to determine the coordination environment and ligand-field parameters of Co^{2+} upon B-site substitution and thermal treatment.

2. Materials and Methods

2.1. Glass Preparation and In Situ Nanocrystal Growth

A borosilicate glass matrix with nominal molar composition $40SiO_2$–$39B_2O_3$–$1Al_2O_3$–$5Cs_2O$–$5PbI_2$–10NaI (mol%) was used as host for the in situ growth of $CsPbI_3$:xCo NCs. Cobalt concentrations of x = 0, 0.05, and 0.10 mol% were defined as the molar fraction of Co^{2+} relative to the total Pb^{2+} content, yielding compositions nominally described as $CsPb_{1-x}Co_xI_3$. All chemical reagents used were nearly 99.0% pure and purchased from Sigma-Aldrich.

Sample preparation followed the fusion method. Stoichiometric amounts of the precursor powders were thoroughly homogenized in an agate mortar and transferred to an alumina crucible. The batch was melted at 1300 °C for 20 min in an electric furnace to ensure complete fusion and chemical homogenization of all precursors. The resulting melt was rapidly quenched onto a preheated stainless-steel plate to suppress uncontrolled crystallization, yielding optically transparent, homogeneous glass discs.

Thermal treatments were subsequently carried out at 500 °C for 6, 10, and 24 h to induce diffusion-driven nucleation and growth of $CsPb_{1-x}Co_xI_3$ NCs within the glass matrix [25]. This

 doi:10.20944/preprints202604.1045.v1

temperature lies near the glass transition temperature (T_g) of the borosilicate host, where short-range atomic mobility of Pb^{2+}, Cs^+, I^-, and Co^{2+} species is sufficient to drive confined crystallization within the rigid vitreous network, enabling controlled NC growth without macroscopic phase segregation or bulk devitrification.

2.2. Structural and Spectroscopic Characterization

The formation, size, shape, and spatial dispersion of the $CsPbI_3$:xCo NCs within the glass matrix were examined by transmission electron microscopy (TEM) using a JEOL JEM-2100 instrument operated at 200 kV. Mean particle diameters and size distributions were obtained from statistical analysis of N = 20 NCs per sample condition using the ImageJ software [33]. Energy-dispersive X-ray spectroscopy (EDX), integrated with the TEM column, was used to evaluate the local elemental composition and to verify cobalt incorporation into the nanocrystalline regions.

The crystalline structure of the $CsPbI_3$:xCo NCs was identified by X-ray diffraction (XRD) using a Shimadzu XRD-6000 diffractometer with Cu $K\alpha_1$ monochromatic radiation (λ = 1.54056 Å). Diffraction profiles were collected over the angular range of 10°–60° (2θ).

Optical absorption (OA) spectra were recorded in the 190–900 nm range using a Shimadzu UV-2600 double-beam UV–Vis spectrophotometer, with the bare borosilicate glass as reference. Photoluminescence (PL) spectra were obtained under continuous-wave laser excitation at 355 nm (≈ 3.49 eV), with an incident power of 12 mW focused to a spot of approximately 200 μm on the sample surface. The emitted light was collected and dispersed by an Avantes multichannel spectrometer operating in the 200–1100 nm range. All measurements were performed at room temperature.

3. Results and Discussion

3.1. Nanocrystal Morphology and Size Distribution

Figure 1 shows TEM micrographs and corresponding particle size distribution histograms of $CsPbI_3$ NCs grown in the borosilicate glass matrix after thermal treatment at 500 °C for 6(a), 10(b), and 24(c) h. In all conditions, discrete nanometric domains are clearly resolved within the amorphous matrix, exhibiting quasi-spherical morphology. The well-defined contrast between the NCs and the surrounding glass host is consistent with the higher electron density of the $CsPbI_3$ phase relative to the borosilicate matrix, confirming successful in situ crystallization [25,26,29].

Statistical analysis of N = 20 NCs per condition shows a systematic increase in mean diameter from 6.3 nm (6 h) to 7.0 nm (10 h) and 8.4 nm (24 h), corresponding to a total size increment of ~33% over the annealing window. The size distributions are unimodal at all three annealing times, indicating that NC growth proceeds without detectable secondary nucleation events [25,29]. The width of the size distributions broadens progressively with annealing time, as directly observable in the histograms of Figure 1, consistent with diffusion-mediated growth in which larger NCs develop preferentially within the glass matrix [27,29].

The monotonic enlargement of NCs with annealing time demonstrates that thermal treatment at 500 °C sustains continued mass transport at the NC–glass interface, driven by the residual atomic mobility available near T_g [25,26]. The unimodal character of the distributions at all annealing times is indicative of a growth regime dominated by the progressive incorporation of diffusing ionic species (Pb^{2+}, Cs^+, I^-) into pre-existing nuclei, rather than by renewed burst nucleation [29]. Even after 24 h of annealing, the NCs remain confined below 10 nm, showing that the rigid borosilicate network effectively restricts long-range ionic diffusion and limits excessive coarsening [25,26,29]. This size range places all samples within or near the quantum confinement regime of $CsPbI_3$, whose exciton Bohr radius is estimated at ~3–4 nm [30], and is directly relevant to the optical properties discussed in Section 3.4.

 doi:10.20944/preprints202604.1045.v1

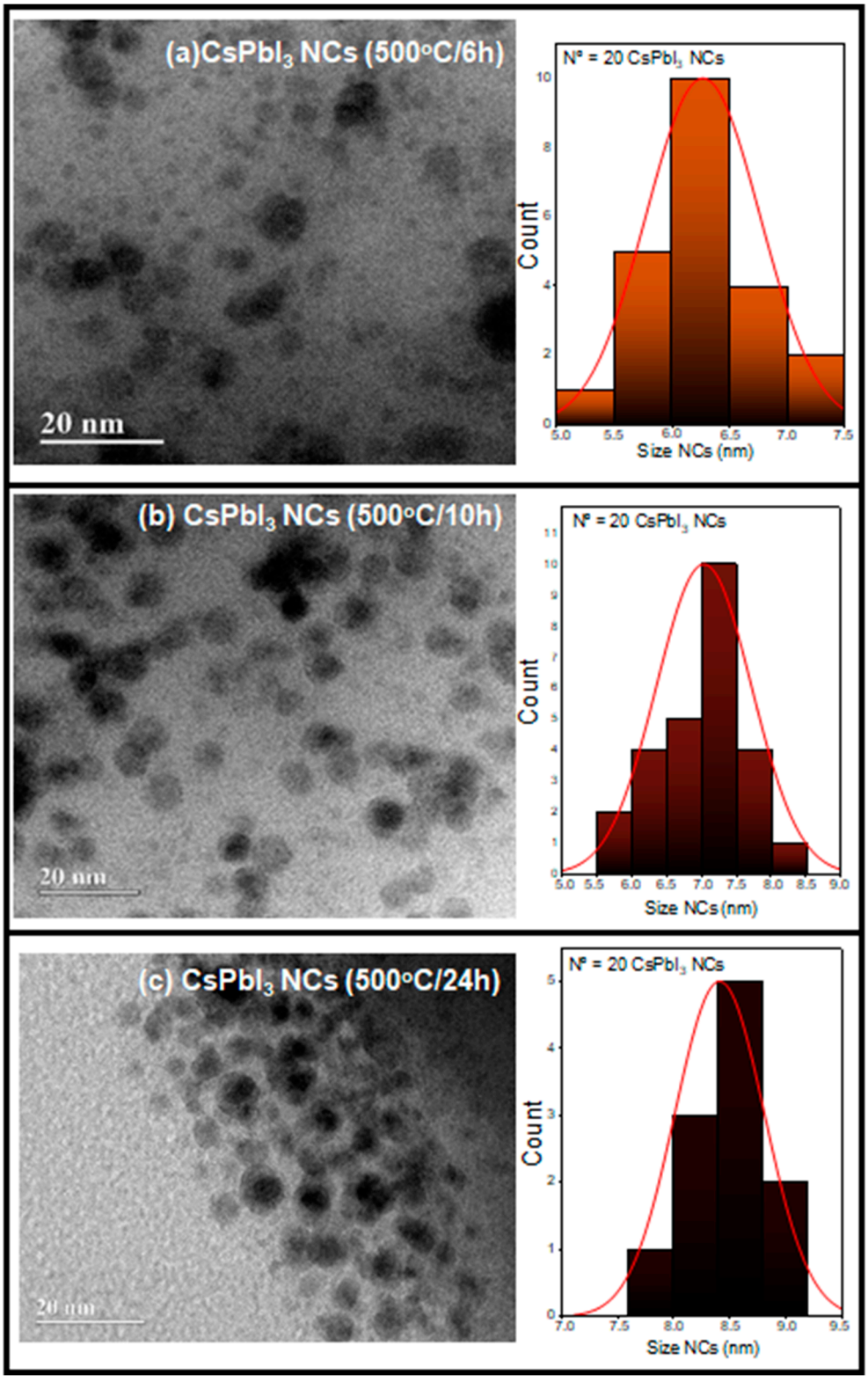

Figure 1. TEM micrographs and corresponding particle size distribution histograms of $CsPbI_3$ NCs grown in a borosilicate glass matrix after thermal treatment at 500 °C for (a) 6 h, (b) 10 h, and (c) 24 h. Mean diameters are 6.3, 7.0, and 8.4 nm, respectively. The systematic size increase and progressive broadening of the distributions with annealing time are consistent with diffusion-mediated growth under glass nanoconfinement.

3.2. Structural Analysis by X-Ray Diffraction

Figure 2(a) shows the XRD patterns of $CsPbI_3$, $CsPbI_3$:5Co, and $CsPbI_3$:10Co NCs grown in the borosilicate glass matrix after thermal treatment at 500 °C for 24 h, corresponding to the condition of maximum NC size established in Section 3.1. All diffractograms display a broad halo centered near

 doi:10.20944/preprints202604.1045.v1

22°–25°, characteristic of the amorphous borosilicate glass host, superimposed by well-resolved Bragg reflections indexed exclusively to the cubic α-$CsPbI_3$ phase (space group Pm3̄m, JCPDS No. 16-1481) [9,13,25,26]. The diffraction peaks observed at approximately 14.2°, 20.1°, 24.5°, 28.3°, 31.8°, 40.5°, and 50.1° are assigned to the (100), (110), (111), (200), (210), (220), and (222) crystallographic planes, respectively. No additional reflections attributable to the orthorhombic δ-$CsPbI_3$ phase, cobalt iodide (CoI_2), or cobalt oxide secondary phases are detected in any of the patterns, confirming that the thermal treatment protocol selectively stabilizes the cubic α-phase across all compositions and that Co^{2+} incorporation does not induce phase separation [9,10,23,27].

Figure 2(b) shows a magnified view of the (200) reflection for the three compositions. A systematic shift of the peak maximum toward higher 2θ values is observed with increasing cobalt content, from 28.27° (d_{200} ≈ 0.3161 nm) in $CsPbI_3$ to approximately 28.29° (d_{200} ≈ 0.3154 nm) in $CsPbI_3$:5Co and, 28.32° (d_{200} ≈ 0.3151 nm) in $CsPbI_3$:10Co. According to Bragg's law ($n\lambda = 2d \sin\theta$), a shift toward higher diffraction angles at constant wavelength implies a reduction in the interplanar spacing d_{200} and, consequently, a contraction of the cubic unit cell parameter. This behavior is consistent with the formation of a substitutional solid solution across the composition range studied, without evidence of phase coexistence or segregation [12,14,27].

The observed lattice contraction is attributed to the partial substitution of Pb^{2+} (ionic radius ≈ 1.19 Å in 6-fold coordination) by Co^{2+} ions (ionic radius ≈ 0.72 Å in tetrahedral coordination) at the B-site of the ABX_3 perovskite structure. Upon B-site incorporation, Co^{2+} adopts a tetrahedral coordination geometry (T_d) rather than the octahedral environment (O_h) of Pb^{2+}, inducing local distortion of the cubic network and the observed unit cell contraction [20,27]. The systematic reduction in lattice parameter with increasing x is consistent with Vegard's law behavior reported for analogous transition-metal-doped lead halide perovskite systems [23,27]. The local structural distortion introduced by Co^{2+} in T_d geometry is expected to modify the B–X bonding framework and contribute to the thermodynamic stabilization of the cubic α-phase [10,12,14].

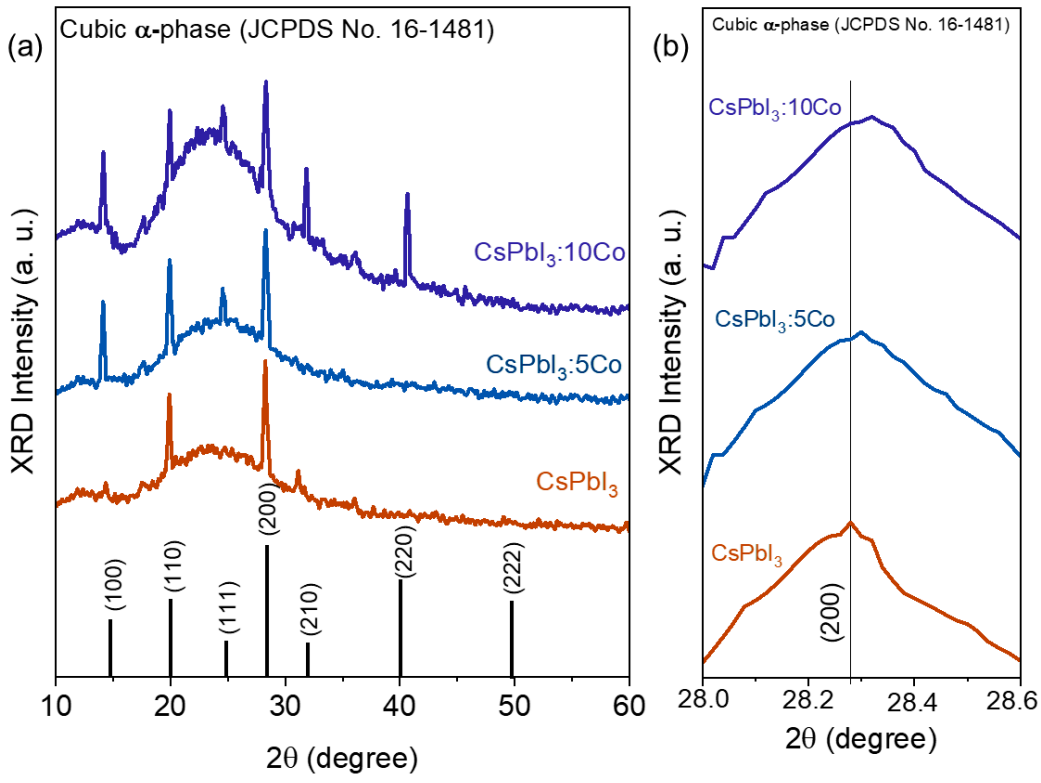

Figure 2. XRD patterns of $CsPbI_3$, $CsPbI_3$:5Co, and $CsPbI_3$:10Co NCs grown in a borosilicate glass matrix after thermal treatment at 500 °C for 24 h. (a) Diffraction profiles showing Bragg reflections indexed exclusively to the cubic α-$CsPbI_3$ phase (space group Pm3̄m, JCPDS No. 16-1481), superimposed on the broad amorphous halo of

 doi:10.20944/preprints202604.1045.v1

the glass host. (b) Enlarged view of the (200) reflection showing the systematic shift to greater 2θ values with increasing Co^{2+} content, evidencing B-site lattice contraction consistent with substitutional incorporation of Co^{2+}.

3.3. Compositional Analysis by TEM–EDX

Figure 3 shows representative TEM micrographs and corresponding EDX spectra of $CsPbI_3$, $CsPbI_3$:5Co, and $CsPbI_3$:10Co NCs subjected to thermal treatment at 500 °C for 10 h. The micrographs confirm the formation of NCs dispersed within the borosilicate glass matrix, displaying quasi-spherical morphology and mean diameters on the order of ~7 nm [25,26], in agreement with the size distributions established in Section 3.1 for this annealing condition. Across all three compositions, the NC morphology and spatial distribution remain essentially unchanged, showing that Co^{2+} incorporation at concentrations up to 0.10 mol% does not measurably affect nucleation density, growth kinetics, or particle morphology under the selected thermal treatment parameters [27,29].

The EDX spectrum of the undoped sample [Figure 3(a)] shows emission lines assigned to Cs (L_α ≈ 4.3 keV), Pb (M_α ≈ 2.3 keV; L_α ≈ 10.5 keV; L_β ≈ 12.6 keV), and I (L_α ≈ 3.9 keV), confirming the chemical identity of the cubic α-$CsPbI_3$ perovskite phase [25]. An additional signal at ~1.7 keV (Si K_α) is attributed to the surrounding borosilicate glass matrix, inevitably sampled by the electron beam given the ~7 nm NC dimensions relative to the probe interaction volume. The prominent Cu Kα signal at ~8 keV originates from the TEM support grid [18,19].

For the Co^{2+}-doped samples [Figure 3 (b) and 3(c)], an additional emission feature appears at approximately 6.9 keV, attributed to the Co K_α transition and highlighted by the blue marker in both spectra. This signal is absent in the undoped reference, confirming cobalt incorporation within the nanocrystalline regions [19,20,27]. The dominant Si K_α signal observed in the doped sample spectra reflects the unavoidable contribution of the borosilicate matrix to the interaction volume, a common limitation in EDX characterization of sub-10 nm NCs embedded in oxide glass matrices [18,29]. No emission lines assignable to CoI_2 or cobalt oxide secondary phases are detected in any spectrum, consistent with the XRD results of Section 3.2 [20,23].

EDX analysis in TEM mode yields spatially averaged compositional information from a region substantially larger than an individual NC and does not independently resolve crystallographic site occupancy or the formal oxidation state of cobalt. Taken together with the XRD results of Section 3.2, specifically the systematic (200) peak shift indicative of B-site lattice contraction, the EDX data support the incorporation of Co^{2+} within the cubic α-$CsPbI_3$ nanocrystalline regions rather than segregation into a separate cobalt-rich phase [20,23,27].

 doi:10.20944/preprints202604.1045.v1

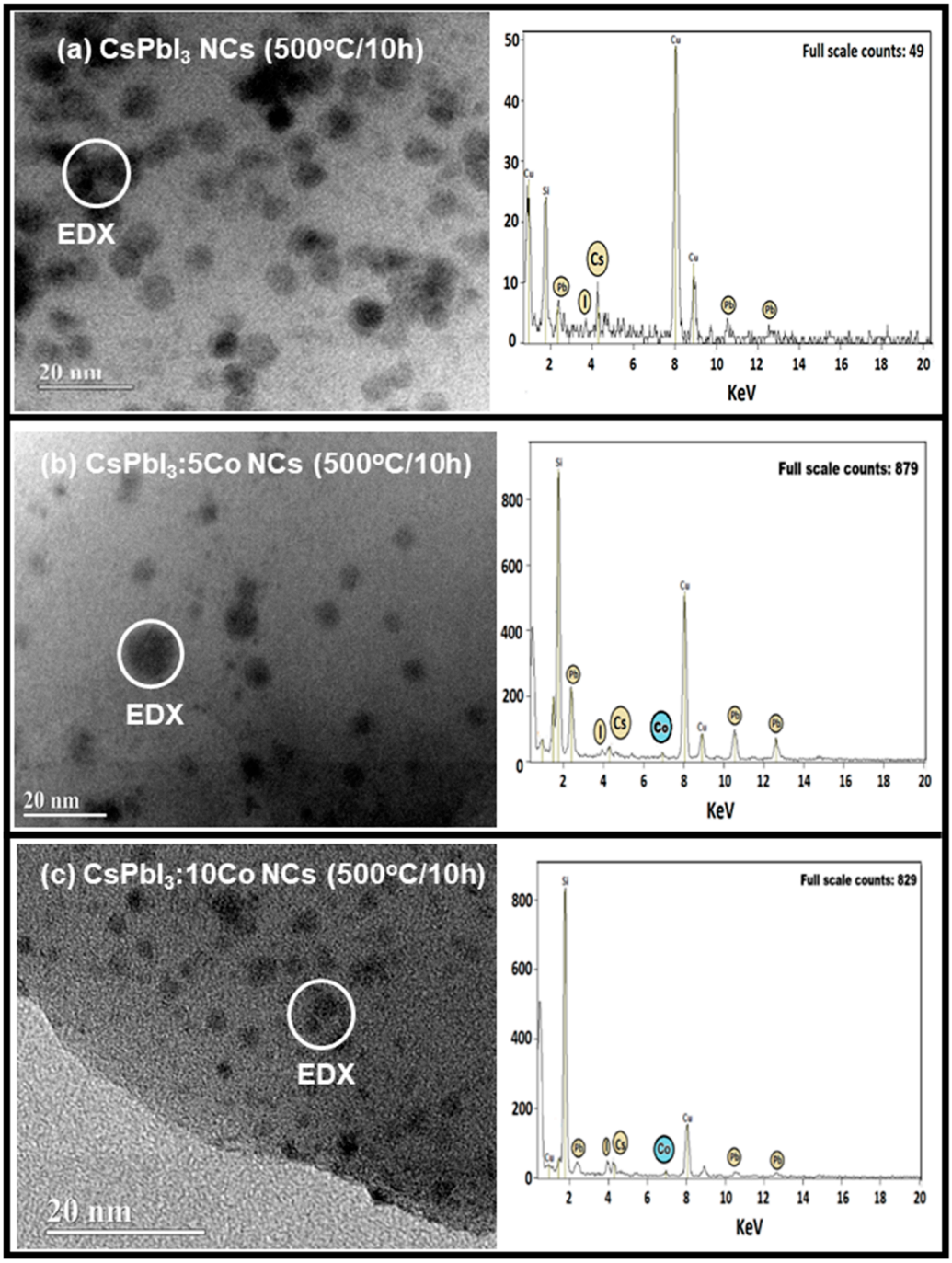

Figure 3. TEM micrographs and corresponding EDX spectra of $CsPbI_3$, $CsPbI_3$:5Co, and $CsPbI_3$:10Co NCs grown in a borosilicate glass matrix after thermal treatment at 500 °C for 10 h: (a) x = 0, (b) x = 0.05, and (c) x = 0.10 mol%. The Co Kα signal at ~6.9 keV is absent in the undoped sample and detected in both Co^{2+}-doped compositions, confirming cobalt incorporation within the nanocrystalline regions without evidence of cobalt-rich secondary phases.

3.4. Optical Properties and Crystal-Field Analysis

Figure 4 shows the OA and PL spectra of $CsPbI_3$, $CsPbI_3$:5Co, and $CsPbI_3$:10Co NCs grown in the borosilicate glass matrix after thermal treatment at 500 °C for 0, 6, 10, and 24 h. The spectral evolution gives simultaneous access to two distinct electronic subsystems: the extended band states of the $CsPbI_3$ host, which govern the excitonic response, and the localized intra-3d levels of Co^{2+}, which reflect the crystal-field environment at the dopant site [7,9,17].

 doi:10.20944/preprints202604.1045.v1

In the as-prepared condition (0 h), the OA and PL spectra of the undoped $CsPbI_3$ sample are characteristic of the δ-phase. The absorption onset is located near 430 nm, consistent with the wide optical bandgap of the δ-phase (~2.8 eV) [9,14], and the PL spectrum shows a broad emission band centered near ~565 nm, attributed to radiative recombination within δ-phase nanocrystallites [9,25]. In the Co^{2+}-doped samples at 0 h, three absorption bands are clearly resolved in the OA spectra, superimposed on the δ-phase background, and their intensities scale with cobalt concentration. Concurrently, the δ-phase PL emission also increases in intensity with Co^{2+} content. This behavior is consistent with a defect-passivation mechanism, in which Co^{2+} ions occupy structural defect sites within the δ-phase nanocrystallites, improving local crystallographic order and thereby enhancing radiative recombination efficiency [18,19].

The three absorption bands observed at 0 h are characteristic of Co^{2+} ($3d^7$) ions in tetrahedral coordination (T_d), consistent with the local reordering of Co^{2+} upon B-site substitution established in Section 3.2 and with the well-documented preference of Co^{2+} for T_d symmetry in halide environments [17,18,36]. Based on the Tanabe–Sugano analysis presented in Figure 5 (lower panel), these bands are assigned as follows: the feature at 15385 cm^{-1} (650 nm) is attributed to the spin-forbidden $^4A_2(^4F) \rightarrow {}^2T_2(^2H)$ transition; the band at 17391 cm^{-1} (575 nm) corresponds to the spin-allowed $^4A_2(^4F) \rightarrow {}^4T_1(^4P)$ transition, consistent with its comparatively greater oscillator strength [17,21,36]; and the higher-energy feature at 20000 cm^{-1} (500 nm) is assigned to the spin-forbidden $^4A_2(^4F) \rightarrow {}^2T_1(^2G)$ transition. The coexistence of one spin-allowed and two spin-forbidden transitions is consistent with a high-spin d^7 configuration in a weak T_d ligand field, as expected for Co^{2+} in iodide-rich coordination [17,28,36].

Upon thermal treatment at 500 °C for 6 and 10 h, the OA and PL spectra show systematic evolution in all compositions. In the undoped $CsPbI_3$ sample, the absorption edge progressively shifts toward longer wavelengths and a narrow, high-intensity excitonic PL band assigned to band-edge recombination of the cubic α-$CsPbI_3$ phase is stabilized at 694 nm (6 h) and 707 nm (10 h) [9,13,25]. This spectral evolution directly reflects NC growth and progressive stabilization of the cubic α-phase established in Sections 3.1, 3.2, and 3.3. Given that the exciton Bohr radius of $CsPbI_3$ is estimated at ~3–4 nm and the NCs span 6.3–8.4 nm, intermediate quantum confinement is operative during the early annealing stages [30]. As the NCs grow, confinement effects are progressively relaxed, contributing to the observed redshift of the excitonic emission. In the Co^{2+}-doped samples at 6–10 h, the α-phase excitonic emission appears at 700–707 nm for $CsPbI_3$:5Co, where PL intensity is attenuated relative to the undoped reference, and at 695–698 nm for $CsPbI_3$:10Co, where PL intensity increases considerably. The enhanced PL intensity observed for $CsPbI_3$:10Co at these intermediate annealing times may be tentatively related to modifications in the quantum confinement regime induced by Co^{2+} incorporation at the B-site. However, a definitive mechanistic assignment requires systematic size-dependent optical studies and is beyond the scope of the present work.

After thermal treatment at 500 °C for 24 h, the excitonic PL emission stabilizes at 712 nm for $CsPbI_3$, 713 nm for $CsPbI_3$:5Co, and 715 nm for $CsPbI_3$:10Co, with PL maxima near ~1.74 eV across all compositions, confirming that Co^{2+} incorporation at the concentrations studied preserves the fundamental optical response of the cubic α-$CsPbI_3$ host [9,25,30]. Concurrently, the Co^{2+} absorption bands, clearly resolved at earlier annealing stages, become progressively masked in the 24 h spectra. This attenuation is attributed to the growth of α-$CsPbI_3$ NCs, whose absorption edge shifts toward ~690 nm with increasing annealing time, reflecting relaxation of quantum confinement. As the band edge of the glass-NC composite progressively covers the visible spectral region, the Co^{2+} intra-3d bands are spectrally overlapped by the rising absorption background, reducing their visibility in the OA spectra [25,30].

Following thermal treatment (6–24 h), four resolved Co^{2+} absorption bands are identified in the OA spectra of the doped samples. Based on the Tanabe–Sugano diagram in Figure 5 (upper panel), these bands are assigned to the transitions $^4A_2(^4F) \rightarrow {}^2E(^2G)$ at 15635 cm^{-1} (630 nm), $^4A_2(^4F) \rightarrow {}^4T_1(^4P)$ at 17094 cm^{-1} (585 nm), $^4A_2(^4F) \rightarrow {}^2T_1(^2G)$ at 18182 cm^{-1} (550 nm), and $^4A_2(^4F) \rightarrow {}^2T_2(^2G)$ at 20202 cm^{-1} (495 nm). The collective blueshift of all transitions relative to the as-prepared state reflects

 doi:10.20944/preprints202604.1045.v1

modifications in the Co^{2+} coordination environment associated with lattice reorganization during α-phase stabilization.

Crystal field theory and Tanabe–Sugano analysis for a d^7 ion in T_d symmetry (Figure 5) yielded, for the as-prepared state (0 h), $\Delta = 5032$ cm^{-1}, $B = 725$ cm^{-1}, $\Delta/B = 6.94$, and $C/B = 4.5$. This Δ/B ratio places the system within the high-spin domain, confirming the thermodynamic stability of the $^4A_2$ ground state and the absence of spin crossover toward a low-spin configuration [17]. The nephelauxetic ratio $\beta = B/B_0 = 725/1120 \approx 0.65$, taking the free-ion Racah parameter $B_0 = 1120$ cm^{-1} for Co^{2+} [36], reflects significant expansion of the Co^{2+} 3d electron cloud due to covalent delocalization into iodide ligand orbitals, consistent with the high polarizability of I^- and its capacity for pronounced metal–ligand orbital overlap [31,32,36–38].

After thermal treatment (6–24 h), the crystal-field parameters evolve to $\Delta = 4428$ cm^{-1}, $B = 805$ cm^{-1}, $\Delta/B = 5.50$, and $\beta = 0.72$. Two correlated changes underlie this evolution. The decrease in Δ (5032 → 4428 cm^{-1}) reflects a weakening of the crystal-field splitting experienced by Co^{2+}, consistent with a slight increase in the average Co–I bond distance as the surrounding lattice reorganizes upon α-phase stabilization [17,28,36]. The increase in B (725 → 805 cm^{-1}), evidenced by the rise in β (0.65 → 0.72), indicates a partial reduction of metal–ligand covalency and a contraction of the effective 3d orbital radius, interpreted as a relaxation of Co–I bond strain as the perovskite lattice approaches its equilibrium cubic structure [18,27,38]. Throughout this evolution, the system remains in the high-spin regime, confirming the preservation of the $^4A_2$ ground state.

The OA, PL, and crystal-field data show that the optical and structural properties of glass-confined $CsPbI_3$:xCo NCs are governed by the coexistence of delocalized excitonic states of the α-perovskite lattice and localized 3d crystal-field excitations of Co^{2+} [17,18,38]. Thermal treatment controls α-phase stabilization, confinement relaxation, and the redistribution of Co^{2+} coordination environments, as directly read from the evolution of Δ and β.

 doi:10.20944/preprints202604.1045.v1

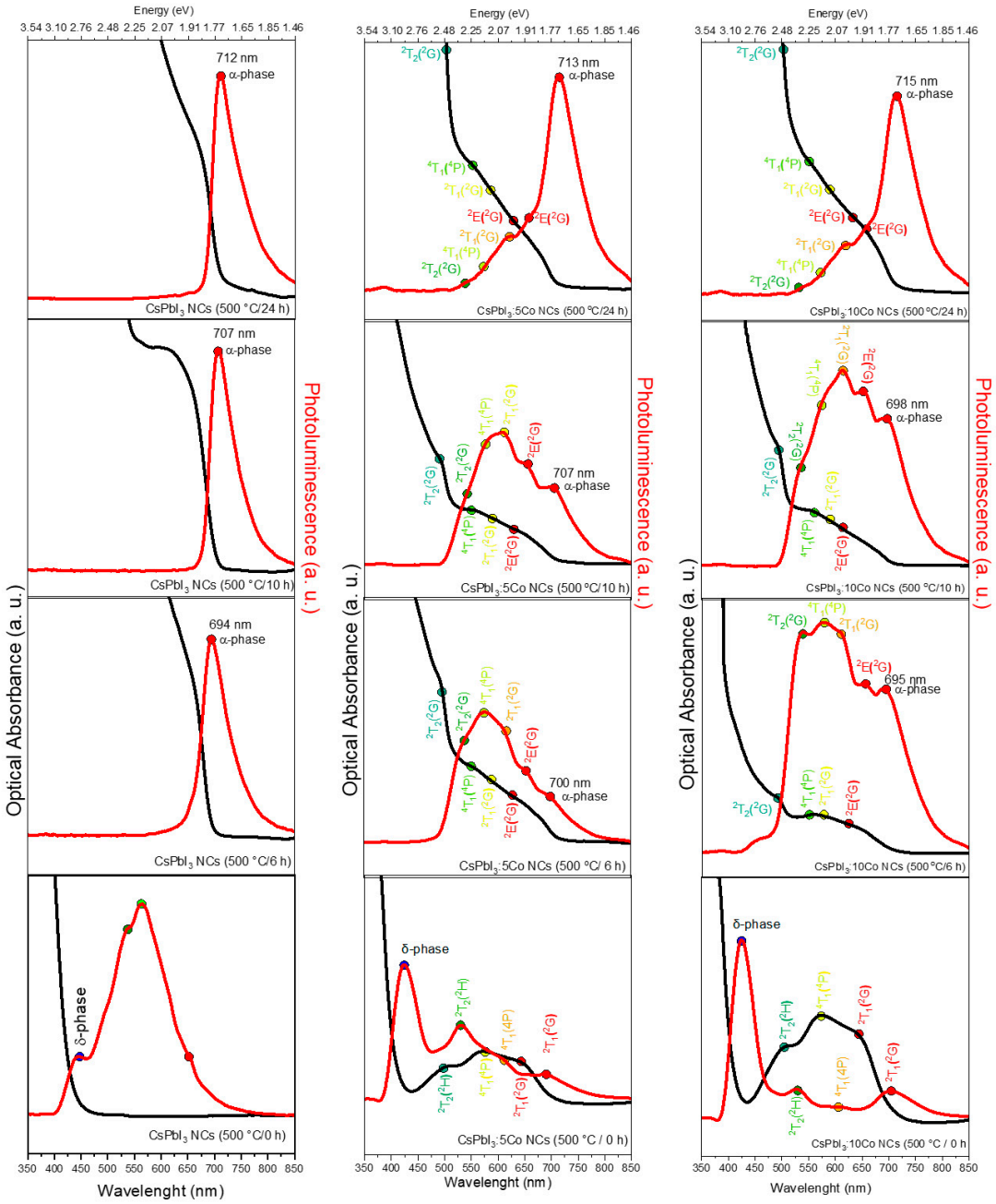

Figure 4. OA (black curves) and PL (red curves) spectra of $CsPbI_3$, $CsPbI_3$:5Co, and $CsPbI_3$:10Co NCs grown in a borosilicate glass matrix after thermal treatment at 500 °C for 0, 6, 10, and 24 h. In the undoped sample, the absorption edge and band-edge excitonic emission progressively redshift with annealing time, reflecting NC growth, relaxation of quantum confinement, and progressive stabilization of the cubic α-$CsPbI_3$ phase. In the Co^{2+}-doped samples, additional absorption bands assigned to the $^4A_2(^4F) \rightarrow {}^2T_2(^2H)$, $^4A_2(^4F) \rightarrow {}^4T_1(^4P)$, and $^4A_2(^4F) \rightarrow {}^2T_1(^2G)$ crystal-field transitions of tetrahedrally coordinated Co^{2+} are resolved in the as-prepared condition (0 h), evolving to four bands assigned to $^4A_2(^4F) \rightarrow {}^2E(^2G)$, $^4A_2(^4F) \rightarrow {}^4T_1(^4P)$, $^4A_2(^4F) \rightarrow {}^2T_1(^2G)$, and $^4A_2(^4F) \rightarrow {}^2T_2(^2G)$ after thermal treatment.

 doi:10.20944/preprints202604.1045.v1

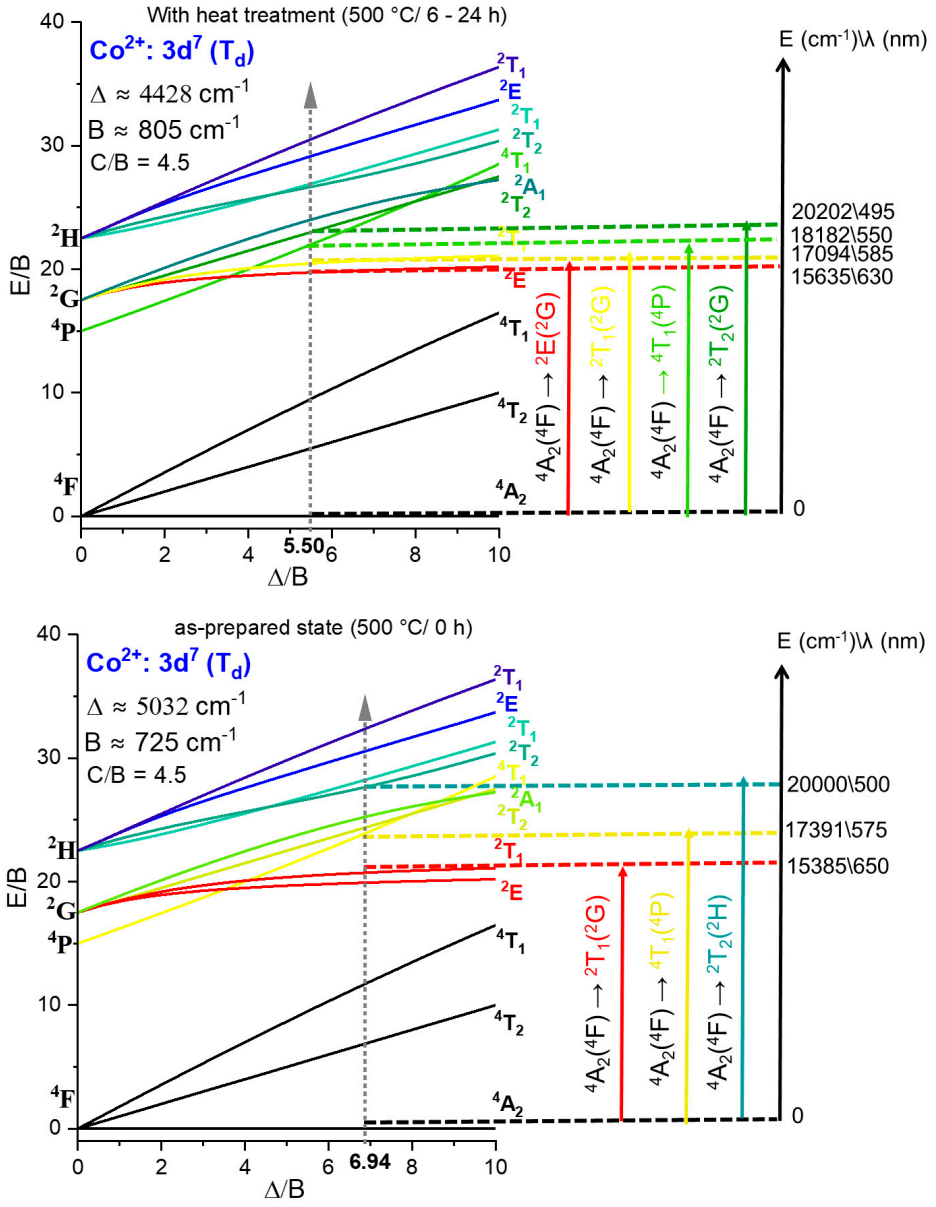

Figure 5. Tanabe–Sugano diagrams for Co^{2+} ($3d^7$, T_d symmetry, C/B = 4.5) in the as-prepared state (500 °C, 0 h; lower panel) and after thermal treatment (500 °C, 6–24 h; upper panel). In the as-prepared state, the crystal-field parameters Δ = 5032 cm^{-1}, B = 725 cm^{-1}, and Δ/B = 6.94 are extracted from the $^4A_2(^4F) \rightarrow {}^2T_2(^2H)$, $^4A_2(^4F) \rightarrow {}^4T_1(^4P)$, and $^4A_2(^4F) \rightarrow {}^2T_1(^2G)$ transitions. After thermal treatment, four transitions are resolved and the parameters evolve to Δ = 4428 cm^{-1}, B = 805 cm^{-1}, and Δ/B = 5.50, reflecting weakening of the crystal-field splitting and partial reduction of metal–ligand covalency associated with lattice reorganization upon α-phase stabilization.

4. Conclusions

$CsPbI_3$:xCo (x = 0, 0.05, and 0.10 mol%) NCs were synthesized in situ within a borosilicate glass matrix by the fusion method followed by controlled thermal treatment at 500 °C for 6–24 h. TEM images showed quasi-spherical NCs with mean diameters increasing from 6.3 to 8.4 nm with annealing time, exhibiting unimodal size distributions consistent with diffusion-mediated growth under glass nanoconfinement. XRD patterns confirmed the exclusive stabilization of the cubic α-phase across all compositions. A systematic shift of the (200) reflection to greater angles with increasing Co content was observed, attributed to B-site substitution of Pb^{2+} (≈ 1.19 Å) by Co^{2+} (≈ 0.72 Å), which adopts tetrahedral coordination (T_d) upon incorporation, inducing local distortion of the cubic network without secondary phase formation. EDX analysis confirmed cobalt incorporation within the nanocrystalline regions. OA and PL spectra showed that Co^{2+} incorporation in the as-

 doi:10.20944/preprints202604.1045.v1

prepared condition enhances the δ-phase emission intensity, consistent with defect passivation within the δ-phase nanocrystallites. Upon thermal treatment, progressive stabilization of the cubic α-phase is accompanied by consolidation of band-edge excitonic emission near ~1.74 eV across all compositions, confirming that Co^{2+} preserves the fundamental optical response of the α-$CsPbI_3$ host. Crystal field theory and Tanabe–Sugano analysis for d^7 ions in Td symmetry yielded $\Delta = 5032\ cm^{-1}$, $B = 725\ cm^{-1}$, and $\beta \approx 0.65$ in the as-prepared state, evolving to $\Delta = 4428\ cm^{-1}$, $B = 805\ cm^{-1}$, and $\beta \approx 0.72$ after thermal treatment, confirming a stable high-spin d^7 configuration and significant Co^{2+}–iodide covalency. The collective blueshift of Co^{2+} transitions reflects lattice reorganization upon α-phase stabilization. The optical and structural data show that the properties of $CsPbI_3$:xCo NCs in borosilicate glass are governed by the coexistence of delocalized excitonic states of the α-$CsPbI_3$ host and localized 3d crystal-field excitations of Co^{2+} in Td symmetry, offering a robust glass-integrated system for photonic applications.

Author Contributions: Wilson A. da Silva: Resources, Methodology, Investigation, Writing – review and editing. Éder V. Guimarães: Resources, Methodology, Investigation, Writing – original draft, Writing – review and editing. Klever A. S. Costa: Resources, Methodology. Nataly S. Moura: Resources, Methodology. José F. Condeles: Resources, Methodology. Raquel A. Domingues: Resources, Methodology, Investigation, Writing – review and editing. Ricardo S. Silva: Resources, Methodology, Investigation, Writing – review and editing.

Funding: The authors gratefully acknowledge financial support from Fundação de Amparo à Pesquisa do Estado de Minas Gerais (FAPEMIG), Conselho Nacional de Desenvolvimento Científico e Tecnológico (PDJ/CNPq 152648/2025-9), and Rede Mineira de Materiais Inorgânicos (RM2I), a research group supported by FAPEMIG (RED–00116–23).

Data Availability Statement: The data that support the findings of this study are available from the corresponding author upon reasonable request.

Acknowledgments: The authors acknowledge the Multi-User Laboratory of High Resolution Microscopy (LabMic) at the Federal University of Goiás for providing access to the TEM facilities used in this work.

Conflicts of Interest: The authors declare no conflicts of interest.

References

1. Abdullah, M.; Obayedullah, M.; Islam Shuvo, M.S.; Khair, M.A.; Hossain, D.; Islam, M.N. A review on multifunctional applications of nanoparticles: Analyzing their multi-physical properties. *Results Surf. Interfaces* **2025**, *21*, 100635. https://doi.org/10.1016/j.rsurfi.2025.100635
2. Parveen, A.; Thakur, P.; Sharma, N.; Kumar, A.S.; Chitra Lekha, C.S.; Kumar, P.; Lal, M. Microstructural, optical, dielectric, and magnetic properties of multifunctional $Zn_{1-x}Fe_xO$ nanoparticles. *J. Opt.* **2024**. https://doi.org/10.1007/s12596-024-02377-w
3. Górska, M.; Kilański, Ł.; Łusakowski, A. Magnetic interactions in IV–VI diluted magnetic semiconductors. *Phys. Status Solidi B* **2022**, *259*, 2100592. https://doi.org/10.1002/pssb.202100592
4. Kalita, H.; Bhushan, M.; Robindro Singh, L. A comprehensive review on theoretical concepts, types and applications of magnetic semiconductors. *Mater. Sci. Eng. B* **2023**, *288*, 116201. https://doi.org/10.1016/j.mseb.2022.116201
5. Rastrello, L.R.; Guimarães, E.V.; da Silva, M.A.T.; Dantas, N.O.; Cano, N.F.; Lourenço, S.A.; da Silva, R.S. Effect of thermal annealing and sp-d exchange interaction in the optical properties of Mn2+-doped PbS nanocrystals embedded in a glass matrix. *J. Lumin.* **2020**, *222*, 117144. https://doi.org/10.1016/j.jlumin.2020.117144
6. Ciechan, A.; Bogusławski, P. Theory of the sp–d coupling of transition metal impurities with free carriers in ZnO. *Sci. Rep.* **2021**, *11*, 3848. https://doi.org/10.1038/s41598-021-83258-1
7. Li, X.; Cao, F.; Yu, D.; Chen, J.; Sun, Z.; Shen, Y.; Zhu, Y.; Wang, L.; Wei, Y.; Wu, Y.; et al. All inorganic halide perovskites nanosystem: Synthesis, structural features, optical properties and optoelectronic applications. *Small* **2017**, *13*, 1603996. https://doi.org/10.1002/smll.201603996

 doi:10.20944/preprints202604.1045.v1

8. Wang, J.; Che, Y.; Duan, Y.; Liu, Z.; Yang, S.; Xu, D.; Fang, Z.; Lei, X.; Li, Y.; Liu, S. 21.15%-efficiency and stable γ-$CsPbI_3$ perovskite solar cells enabled by an acyloin ligand. *Adv. Mater.* **2023**, *35*, 2210223. https://doi.org/10.1002/adma.202210223
9. Jin, H.; Zeng, Y.-J.; Steele, J.A.; Roeffaers, M.B.J.; Hofkens, J.; Debroye, E. Phase stabilization of cesium lead iodide perovskites for use in efficient optoelectronic devices. *NPG Asia Mater.* **2024**, *16*, 24. https://doi.org/10.1038/s41427-024-00540-0
10. Ke, F.; Wang, C.; Jia, C.; Wolf, N.R.; Yan, J.; Niu, S.; Devereaux, T.P.; Karunadasa, H.I.; Mao, W.L.; Lin, Y. Preserving a robust CsPbI3 perovskite phase via pressure-directed octahedral tilt. *Nat. Commun.* **2021**, *12*, 461. https://doi.org/10.1038/s41467-020-20745-5
11. Kralj, S.; Morales-Masis, M. Growth and stabilization of cubic $FAPbI_3$: On the interaction between phosphonic acids and co-evaporated perovskites. *Matter* **2024**, *7*, 3238–3240. https://doi.org/10.1016/j.matt.2024.09.007
12. Wang, Q.; Zheng, X.; Deng, Y.; Zhao, J.; Chen, Z.; Huang, J. Stabilizing the α-phase of $CsPbI_3$ perovskite by sulfobetaine zwitterions in one-step spin-coating films. *Joule* **2017**, *1*, 371–382. https://doi.org/10.1016/j.joule.2017.07.017
13. Qi, W.; Liang, H.; Haruta, Y.; Saidaminov, M.I.; Mi, Q.; Saliba, M.; Cui, G.; Ning, Z.; Rasband, W.S. From tetragonal to cubic: Perovskite phase structure evolution for high-performance solar cells. *Sci. Bull.* **2023**, *68*, 141–145. https://doi.org/10.1016/j.scib.2023.01.008
14. Tan, X.; Wang, S.; Zhang, Q.; Liu, H.; Li, W.; Zhu, L.; Chen, H. Stabilizing $CsPbI_3$ perovskite for photovoltaic applications. *Matter* **2023**, *6*, 691–727. https://doi.org/10.1016/j.matt.2022.12.012
15. González, J.E.; Danelon, J.G.; Da Silva, J.L.F.; Lima, M.P. Elucidating black α-$CsPbI_3$ perovskite stabilization via PPD bication-conjugated molecule surface passivation: Ab initio simulations. *ACS Appl. Mater. Interfaces* **2024**, *16*, 39251–39265. https://doi.org/10.1021/acsami.4c05092
16. Alsubaie, F.; Du, A.; Zhang, L. Band edge engineering of $CsPbI_3$ by surface decoration of halogen and alkaline atoms. *Comput. Mater. Sci.* **2025**, *253*, 113863. https://doi.org/10.1016/j.commatsci.2025.113863
17. Jana, Y.; Biswas, A.; Halder, D.; Sarkar, S.; Rudowicz, C. Exploring crystal field influences on optical spectra of $3d^7$ (Ni^{3+} vs Co^{2+}) ions in cubic pyrochlores $A_2Ti_2O_7$ (A = Y, Gd) and layered-hexagonal MCl_2 (M = Cd, Mg) for potential optoelectronic applications. *J. Solid State Chem.* **2025**, *345*, 125241. https://doi.org/10.1016/j.jssc.2025.125241
18. Guimarães, E.V.; Silva, A.S.; Azevedo, G.A.; Dantas, N.O.; Silva, R.S. Internal energy transfer from nanocrystals to Co^{2+} ions at Bi_2S_3 tetrahedral sites embedded in host glass. *J. Lumin.* **2023**, *255*, 119517. https://doi.org/10.1016/j.jlumin.2022.119517
19. Guimarães, E.V.; Gonçalves, E.R.; Lourenço, S.A.; Oliveira, L.C.; Baffa, O.; Silva, A.C.A.; Dantas, N.O.; Silva, R.S. Concentration effect on the optical and magnetic properties of Co^{2+}-doped Bi_2S_3 semimagnetic nanocrystals growth in glass matrix. *J. Alloys Compd.* **2018**, *740*, 974–979. https://doi.org/10.1016/j.jallcom.2018.01.073
20. Silva, R.S.; Guimarães, E.V.; Melo, R.E.S.; Silva, A.S.; Silva, A.C.A.; Dantas, N.O.; Lourenço, S.A. Investigation of structural and optical properties of $Pb_{1-x}Co_xS$ nanocrystals embedded in chalcogenide glass. *Mater. Chem. Phys.* **2021**, *269*, 124766. https://doi.org/10.1016/j.matchemphys.2021.124766
21. Batista, E.A.; Silva, A.C.A.; Rezende, T.K.; Guimarães, E.V.; Pereira, P.A.G.; Souza, P.E.N.; Silva, R.S.; Morais, P.C.; Dantas, N.O. Modulating the magnetic-optical properties of $Zn_{1-x}Co_xO$ nanocrystals with x-content. *J. Mater. Res.* **2021**, *36*, 1657–1665. https://doi.org/10.1557/s43578-021-00162-0
22. Silva, A.S.; Lourenço, S.A.; Da Silva, M.A.T.; Da Silva, S.W.; Morais, P.C.; Dantas, N.O. Effect of Co co-doping on the optical properties of ZnTe:Mn nanocrystals. *Phys. Chem. Chem. Phys.* **2017**, *19*, 1158–1166. https://doi.org/10.1039/C6CP05866C
23. Bhat, A.A.; Khandy, S.A.; Islam, I.; et al. Optical, electrochemical and photocatalytic properties of cobalt doped $CsPbCl_3$ nanostructures: A one-pot synthesis approach. *Sci. Rep.* **2021**, *11*, 16473. https://doi.org/10.1038/s41598-021-95088-2
24. Noguera-Gómez, J.; Fernández-Guillen, I.; Betancur, P.F.; Chirvony, V.S.; Boix, P.P.; Abargues, R. Low-demanding in situ crystallization method for tunable and stable perovskite nanoparticle thin films. *Matter* **2022**, *5*, 3541–3552. https://doi.org/10.1016/j.matt.2022.07.017

 doi:10.20944/preprints202604.1045.v1

25. Silva, R.S.; Camilo, N.S.; Guimarães, E.V.; Condeles, J.F.; Lourenço, S.A.; Fernandes, R.V.; Andrade, A.A. Optical and structural properties of Er^{3+}-doped $CsPbI_3$ nanocrystals embedded in borosilicate glass. *Physica B* **2025**, *696*, 416646. https://doi.org/10.1016/j.physb.2024.416646
26. Si, S.; Yu, J.; Lou, S.; Lan, B.; Zhang, J.; Zhang, X.; Li, M.-R.; Huang, L.; Wang, J. Engineering the crystallization behavior of $CsPbBr_3$ quantum dots in borosilicate glass through modulating the glass network modifiers for wide-color-gamut displays. *J. Eur. Ceram. Soc.* **2022**, *42*, 3586–3594. https://doi.org/10.1016/j.jeurceramsoc.2022.03.008
27. Li, J.; Hu, D.; Chen, Q. Pb^{2+}/Co^{2+} modified growth and phase transitions of $CsPbBr_3$ in heavy metal oxide glass with enhanced magnetic and magneto-optical properties. *J. Eur. Ceram. Soc.* **2024**, *44*, 2206–2222. https://doi.org/10.1016/j.jeurceramsoc.2023.11.070
28. Raghuvanshi, V.; Rashmi, I.; Ingle, A.; Shashikala, H.D.; Nagaraja, H.S. A study on the influence of geometric coordination of cobalt ions on the structural, physical and optical properties of borosilicate glass. *Ceram. Int.* **2025**, *51*, 1661–1673. https://doi.org/10.1016/j.ceramint.2024.11.142
29. Fonseca, J. Nanoparticles embedded into glass matrices: Glass nanocomposites. *Front. Mater. Sci.* **2022**, *16*, 220607. https://doi.org/10.1007/s11706-022-0607-7
30. Li, Y.; Deng, M.; Zhang, X.; Xu, T.; Wang, X.; Yao, Z.; Wang, Q.; Qian, L.; Xiang, C. Stable and efficient $CsPbI_3$ quantum-dot light-emitting diodes with strong quantum confinement. *Nat. Commun.* **2024**, *15*, 5696. https://doi.org/10.1038/s41467-024-50022-8
31. Xu, H.; Xu, D.C.; Wang, Y. Natural indices for the chemical hardness/softness of metal cations and ligands. *ACS Omega* **2017**, *2*, 7185–7193. https://doi.org/10.1021/acsomega.7b01039
32. Law, S.K. Role of ligand design on the stability of metal complexes and its catalytic properties—A mini-review. *Biointerface Res. Appl. Chem.* **2024**, *14*, 64. https://doi.org/10.33263/BRIAC143.064
33. Schneider, C.A.; Rasband, W.S.; Eliceiri, K.W. NIH Image to ImageJ: 25 years of image analysis. *Nat. Methods* **2012**, *9*, 671–675. https://doi.org/10.1038/nmeth.2089
34. Nadhiya, D.; Kala, A.; Sandhiya, V.; Thirunavukkarasu, P.; Karnan, C.; Prabhaharan, M.; Sasikumar, P.; Albukhaty, S.; Sulaiman, G.M. Influence of annealing temperature on structural, morphological, optical, magnetic, and antimicrobial properties of zinc ferrite nanoparticles. *Plasmonics* **2024**, *19*, 1753–1763. https://doi.org/10.1007/s11468-023-02098-z
35. Očenášek, J.; Minár, J.; Alcalá, J. Dynamics of lattice disorder in perovskite materials, polarization nanoclusters and ferroelectric domain wall structures. *npj Comput. Mater.* **2023**, *9*, 118. https://doi.org/10.1038/s41524-023-01069-6
36. Lourenço, S.A.; Silva, R.S.; Silva, A.C.A.; Dantas, N.O. Structural and optical properties of Co^{2+}-doped PbSe nanocrystals in chalcogenide glass matrix. *J. Phys. Chem. C* **2015**, *119*, 13277–13282. https://doi.org/10.1021/acs.jpcc.5b01920
37. Lourenço, S.A.; Silva, R.S.; Dantas, N.O. Tunable dual emission in visible and near-infrared spectra using Co^{2+}-doped PbSe nanocrystals embedded in a chalcogenide glass matrix. *Phys. Chem. Chem. Phys.* **2016**, *18*, 23036–23043. https://doi.org/10.1039/C6CP04419K
38. Sinha, N.; Yaltseva, P.; Wenger, O.S. The nephelauxetic effect becomes an important design factor for photoactive first-row transition metal complexes. *Angew. Chem. Int. Ed.* **2023**, *62*, e202303864. https://doi.org/10.1002/anie.202303864